On-Chip Optical Vortex Generation and Topological Charge Control by Methods of Wave Vector Manipulation

Jingfu Ye, Yan Li, Yi Liu, and Shiliang Qu

***Abstract*—Optical vortices (OVs) have received much attention in recent years and are widely explored in communication applications. The on-chip vortex emitter/modulator is preferred when it comes to photonic integration and chip-scale communication. However, the existing emitters/modulators suffer from either narrow bandwidths or extensibility problems, which actually degrade their ability to improve communication capacity. Here, we propose a metasurface OV emitter based on wave vector synthesis for vortex generation and modulation. A thorough theoretical analysis of the OV generation by two approximate methods was carried out, which suggests the superiority of Wave Vector method over Phase method. Afterwards, the wave vector manipulation implemented by Phase gradient metasurfaces was studied for controlling the topological charges of generated OVs. Finite element method simulations showed that, in the topological charge range of −6 to 6 and the wavelength range of 1.45 μm to 1.55 μm, the effective vortex emission efficiency of the proposed emitter is around 45%. The on-chip vortex generation and control by wave vector manipulation is a very promising technology for high-capacity inter-chip optical communication.**

***Index Terms*—Integrated photonics, metasurface, optical communication, surface plasmon polaritons, vortex emitting.**

I. Introduction

OPTICAL vortices (OVs) with azimuthal phase dependence $\exp(il\varphi)$ can carry orbital angular momentum (OAM) of $l\bar{h}$ per photon (φ is the transverse azimuthal angle, l is topological charge, $\bar{h}$ is the reduced Planck constant) [1]. They have attracted much attention in recent years [2], and have wide-ranging applications in particle manipulation [3], [4], microfabrication [5], [6], optical communication [7]–[10], and quantum information [11]–[13]. Vortex generation and discrimination are routinely implemented by spatial light modulator (SLM) [7], [9], digital micro-mirror device (DMD) [13], spiral phase plates [14], and metasurfaces [15]–[17]. These optical elements are all designed to manipulating light beams in free-space. An on-chip vortex transceiver is preferred when it comes to photonic integration and chip-scale OV communication. The integrated transceivers are aimed at linking free-space optical vortices and on-chip bounded or guided waves. Such devices can provide new opportunities for widespread application of OVs due to their advantages in reliability, miniaturization, and scalability.

There have seen researches on integrated OV transceivers and their application in OV communication. One effective approach is to use waveguide arrays to discriminate/generate OVs with various topological charges (TCs) [18], [19]. The main drawback of these devices is the heavy and complicated design and the relatively large footprint. Another approach is based on the light coupling between whispering gallery modes and free-space OVs [20], [21]. The structure is compact and the generated phase is accurate. However, the inherent narrow bandwidth of micro-ring resonators hinders the device from being compatible with wavelength-division-multiplexing (WDM) techniques, and thus actually degrades the device's ability to improve communication capacity [22]. Although nano-cavity-based OV emitters have been shown to possess both compactness and broad bandwidths, they suffer an extensibility issue owing to the M-proportional insertion loss (M is the number of OV channels) [22]. Phase gradient metasurfaces (PGMs) may provide a solution. They have been used to manipulate wave vector either in free space or in waveguides [23]–[26]. Here we propose a PGM-based OV transceiver. The PGMs in this device are utilized as bridges linking different free-space OVs with surface plasmon polaritons (SPPs) incident in different directions. The proposed device, with features of compactness, wide bandwidth, large OV channel capacity and capabilities of fast OV modulation, is very promising for inter-chip WDM-compatible OV communication.

Quarter-ring-shaped PGMs (QR-PGMs) are designed to fulfill wave vector matching between OVs and SPPs, as shown in Fig. 1. The structural wave vector of each QR-PGM is directed outward along the corresponding port normal line (black dashed line), and the four QR-PGMs are actually equivalent to each other under a rotation operation around their central vertical line. Four SPPs are fed into QR-PGMs with the same angle α. Specifically, SPPs with $\alpha = 0°$ will result in trivial radiated

Manuscript received October 4, 2021; revised December 11, 2021; accepted January 7, 2022. Date of publication January 14, 2022; date of current version January 31, 2022. This work was supported in part by the National Natural Science Foundation of China under Grants 11874010 and 11874133, and in part by the Natural Science Foundation of Guangxi Province under Grants 2020GXNSFAA238040 and 2021GXNSFAA075012. *(Corresponding author: Shiliang Qu.)*

Jingfu Ye is with the Photonics Research Center, School of Electronic Engineering and Automation, Guilin University of Electronic Technology, Guilin 541004, China (e-mail: jingfu_ye@163.com).

Yan Li and Yi Liu are with the School of Science, Harbin Institute of Technology, Weihai 264209, China (e-mail: liy@hit.edu.cn; shandongliu2006@163.com).

Shiliang Qu is with the Photonics Research Center, School of Electronic Engineering and Automation, Guilin University of Electronic Technology, Guilin 541004, China, and also with the School of Physics, Harbin Institute of Technology, Harbin 150001, China (e-mail: slqu@hit.edu.cn).

Digital Object Identifier 10.1109/JPHOT.2022.3143373

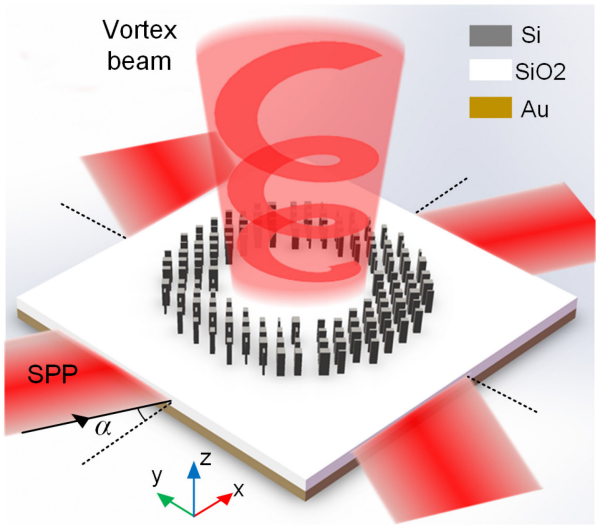

Fig. 1. Schematic diagram of the OV emitter composed of PGMs.

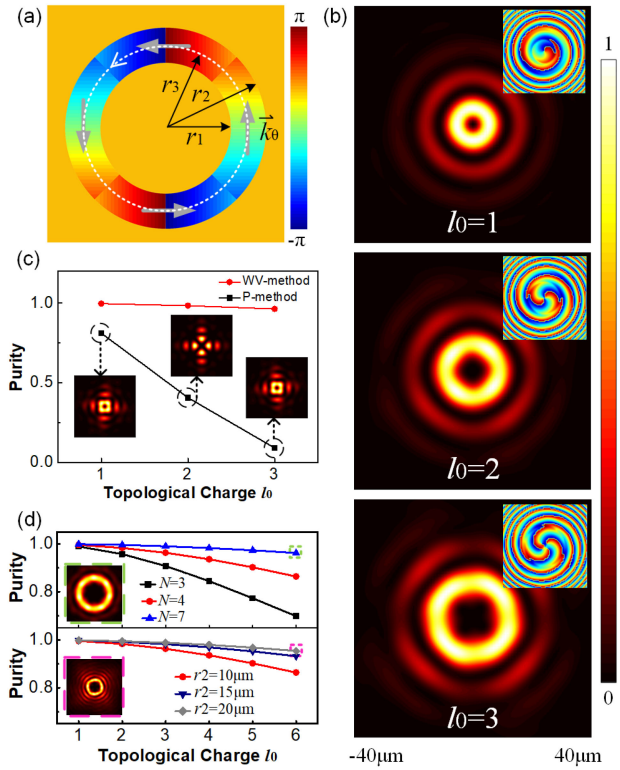

Fig. 2. Mathematical analysis of OV generation. (a) Mechanism of an annular source with the vortex phase discretized by WV-method. (b) Normalized intensities of OVs generated by WV-method. Insets show the phase distributions. (c) Purities of generated OVs. Insets show the intensities of OVs generated by P-method. (d) Dependence of OV purities on the number of segments with $r_2 = 10\ \mu$m (upper panel), and the outside radius of the ring with $N = 4$ (lower panel). Insets show the intensity distributions of generated OVs with $l_0 = 6$.

waves with no phase singularities, while the SPPs with negative and positive α (clockwise and anticlockwise angle) will result in OVs with positive and negative TCs respectively. Reversely, this device can be used as a receiver to decompose OVs into four obliquely outgoing SPPs. In a word, the PGM-based transceiver can be viewed as interfaces between angle and topology coded information. This paper aims to study the mechanism of the OV generation and control implemented by wave vector synthesis, and, based on this, a specific design of OV emitter is provided. First, the methods of vortex generation are discussed, especially the wave vector methods.

II. Methods of Vortex Generation

It is not difficult to show that, an on-plane field source with complex amplitude $u(r,\varphi,z=0) = a(r)\exp(il\varphi)$ could result in an OV with expression $u(r,\varphi,z) = A(r,z)\exp(il\varphi)$ after diffraction, where r, φ and z are cylindrical coordinates, $a(r)$ is an arbitrary amplitude function of r, and $A(r,z)$ is the amplitude resulted from diffraction. In other words, continuous azimuthal phase modulation on plane can ultimately generate ideal vortex beams. Waveguide microring grating is exactly an ideal vortex generator [20], but the inherent ultra-narrow band arising from whispering gallery mode resonance hinders the device from being compatible with WDM techniques, and thus actually degrades the device's ability to improve communication capacity [22]. A natural solution is to break the continuous azimuthal phase modulation and generate OVs approximately by discontinuous phase modulation instead. In fact, such methods of OV generation have been widely used in metasurface researches [15], [16], [27]. One commonly used method is the Phase method (P-method), which discretizes on-plane continuous vortex phase into segmented phases with a certain phase step and azimuthal angle step, and retrieves OVs by means of optical diffraction [15], [27]. P-method can be characterized by phase step $\Delta\Phi(l_0) = 2\pi l_0/N$, where l_0 is the TC of target OVs, and N is the number of segments. The main drawback of P-method is the inherent limit to the TC that generated principal maximum OV can possess (i.e., $-0.5N < l < 0.5N$), owing to the periodicity of phase step: $\Delta\Phi(l_0 + N) = \Delta\Phi(l_0)$. Another method which is not commonly used, however, has no such limitation. We call it the Wave Vector method (WV-method). In this method, the continuous vortex phase of the source field is also discretized into segmented phases in azimuthal direction, but the phase in each equal-sized segment exhibits linear distribution and corresponds to a specific phase gradient or wave vector. WV-method has been used to transform free-space Gaussian beams into high-purity OVs [16]. In this paper, WV-method is adopted to generate OVs.

Consider an annular area on the $z = 0$ plane in cylindrical coordinate system. The vortex phase discretized by WV-method is shown in Fig. 2(a), where yellow areas represent opaque materials. Four segments of linear phase with wave vectors $\boldsymbol{k}_\theta$ (gray arrows) are employed to approximate continuous vortex phase ($l_0 = 2$). The value of $\boldsymbol{k}_\theta$ is taken as $k_\theta = \pi l_0/[4r_3\sin(\pi/4)]$, where $r_3 = (r_1 + r_2)/2$, and r_1 and r_2 are inner and outer radius of ring respectively. More generally, the vortex phase discretized by WV-method can be expressed as:

$$\Phi(\rho,\theta) = n(\theta)\frac{2\pi l_0}{N} + k_\theta \rho \sin\left[\theta - n(\theta)\frac{2\pi}{N}\right], \qquad (1)$$

where ρ and θ are polar coordinates, $k_\theta = \pi l_0/[Nr_3\sin(\pi/N)]$, and $n(\theta)$ is a piecewise function with expression as:

$$n(\theta) = \begin{cases} 0 & 0 \le \theta < \frac{\pi}{N} \\ 1 & \frac{\pi}{N} \le \theta < \frac{\pi+2\pi}{N} \\ \vdots & \\ N-1 & \frac{\pi+(N-2)2\pi}{N} \le \theta < \frac{\pi+(N-1)2\pi}{N} \\ 0 & \frac{\pi+(N-1)2\pi}{N} \le \theta < 2\pi \end{cases}. \quad (2)$$

As for amplitude, the piecewise function $f(\rho)$ is adopted, and expressed as:

$$f(\rho) = \begin{cases} 0 & \rho < r_1, \rho > r_2 \\ 1 & r_1 \le \rho \le r_2 \end{cases}. \quad (3)$$

At this point, free-space OVs can be reconstructed by the diffraction from annular source $E(\rho,\theta) = f(\rho)\exp[\mathrm{i}\Phi(\rho,\theta)]$. Based on Rayleigh-sommerfeld diffraction formula [28], [29], the transverse component of electric field in space of $z > 0$ is calculated as:

$$E_t(r,\varphi,z) = \frac{1}{2\pi}\int_0^\infty \int_0^{2\pi} \frac{z(1-\mathrm{i}kR)\exp(\mathrm{i}kR)}{R^3} \times E(\rho,\theta)\rho d\theta d\rho \quad (4)$$

where r, φ and z are cylindrical coordinates, $R = [r^2 + \rho^2 - 2r\rho\cos(\theta - \varphi) + z^2]^{1/2}$, $k = 2\pi/\lambda$, and λ is the wavelength which is determined as 1.55 μm. The diffraction intensities of annular sources with parameters $\{N = 4,\ r_1 = 6.5\ \mu\mathrm{m},\ r_2 = 10\ \mu\mathrm{m}\}$ are shown in Fig. 2(b). They were calculated at $z = 100\ \mu$m and presented in an area of 80 μm × 80 μm (throughout this paper, unless otherwise specified, all diffraction patterns are presented in the same z-position and the same area by default). The doughnut-like shape along with vortex phase (insets in the upper right corner) indicates clearly the generation of OVs.

To make a quantitative analysis, the diffraction field $E_t(r, \varphi, z)$ may be expanded into Fourier series of $\exp(\mathrm{i}l\varphi)$ [30], [31]:

$$E_t(r,\varphi,z) = \frac{1}{\sqrt{2\pi}}\sum_{l=-\infty}^{\infty} a_l(r,z)\exp(il\varphi), \quad (5)$$

where

$$a_l(r,z) = \frac{1}{\sqrt{2\pi}}\int_0^{2\pi} E_t(r,\varphi,z)\exp(-il\varphi)d\varphi, \quad (6)$$

Eq. (5) indicates that the diffraction field $E_t(r,\varphi,z)$ can be regarded as the infinite superposition of vortex beams $E_{lt}(r,\varphi,z) = a_l(r,z)\exp(\mathrm{i}l\varphi)$ with topological charges l. The weight of each vortex harmonic is calculated as:

$$P_l = \int_0^\infty |a_l(r,z)|^2 r\mathrm{d}r \Big/ \int_0^\infty \int_0^{2\pi} |E_t(r,\varphi,z)|^2 r\mathrm{d}\varphi\mathrm{d}r. \quad (7)$$

Here, P_l can be shown to be constants independent of z [30]. P_l can be used for vortex spectrum analysis, and the vortex purity, i.e., weight of target harmonic, can be calculated by substituting $l = l_0$ into (7). The vortex purities of beams in Fig. 2(b) are shown by the red line with dots in Fig. 2(c). They are all higher than 96%. The vortex purities of the beams generated by P-method (black line with squares) were also calculated, which was executed by substituting $k_\theta = 0$ and $l = l_0$ into (7), and by employing parameters equal to that of WV-method. Unsurprisingly, only the beam corresponding to $l_0 = 1$ possesses a vortex purity higher than 50%. The intensity of the beam corresponding to $l_0 = 2$ (inset in the middle) reveals the TC bounds of P-method. In other words, there is just no principal maximum in the vortex spectrum (see Appendix). In the case of $l_0 = 3$, vortex purity is merely 9%. Actually, the principal maximal harmonic possesses the TC of -1, and the diffraction intensity (inset on the right) is the same as that in the case of $l_0 = -1$. It is clear that WV-method is superior to P-method in vortex generation. Vortex purities can be further increased by adjusting two parameters: segment number N and ring size r_2, as shown in Fig. 2(d). Note that the width of ring was determined as a constant of 3.5 μm, and the outside radius r_2 was chosen to represent the ring size. Diffraction beams corresponding to parameters $\{N = 7,\ r_2 = 10\ \mu\mathrm{m}\}$ and parameters $\{N = 4,\ r_2 = 20\ \mu\mathrm{m}\}$ are compared in the case of $l_0 = 6$. Their vortex purities are almost the same, whereas the field intensities (insets in each panel) are distinct from each other. The beam corresponding to larger r_2 closely resembles the diffraction-free Bessel beam which is preferred in OV applications [32], [33]. On the other hand, large N requires more on-chip input ports, which inevitably increases the complexity of optical circuits. Based on these, we recommend the parameters of larger r_2 for high-performance OV generator.

III. Wave Vector Manipulation and Simulation Results

After the mathematical analyses of vortex generation, the PGM-based emitter was investigated through the finite element method (FEM) simulations performed by commercially available COMSOL Multiphysics software [34]. The wavelength $\lambda = 1.55\ \mu$m was investigated, and the refractive indexes of the materials were $n_{\mathrm{Si}} = 3.478$, $n_{\mathrm{SiO2}} = 1.466$, and $n_{\mathrm{Au}} = 0.518 - 10.74\mathrm{i}$.

One quarter of the OV emitter, quarter-ring-truncated PGMs, is shown in Fig. 3(a). Each of its square pixel contains a silicon nanopillar which acts as a local quarter-wave plate (QWP). High-contrast dielectric nanopillars have been widely used in metasurfaces for light phase and polarization control [35], [36]. In the configuration shown in the right panel of Fig. 3(a), the pillar height is $h_3 = 1000$ nm, pillar spacing is $u = 400$ nm, and the orientation angle of silicon pillar is 45°. The length a_1 and width a_2 of the pillar are variable parameters used to manipulate light polarization and phase. To investigate the optical properties of this nanopillar, a full-wave FEM simulation was carried out with non-uniform grid meshes. The periodic boundary condition was adopted, and the minimum mesh size was 10 nm. Based on this, four different pillar dimensions were selected to cover a whole 2π phase change in identical step of $\pi/2$, while simultaneously ensuring the function of QWP. The parameters of the four pillars are listed in Table I. With these blocks, the PGM with structural wave vector $\boldsymbol{k}_{\mathrm{p}}$ was constructed. Its unit cell is shown in the bottom panel of Fig. 3(a). The shape of the unit cell is a square rotated by 45°. The PGM with designed scale is practical with current nanotechnology [35], [36]. It can be seen that the size of the nanopillar increases along the x-direction, which means that the modulated phase increases in the same direction. In other

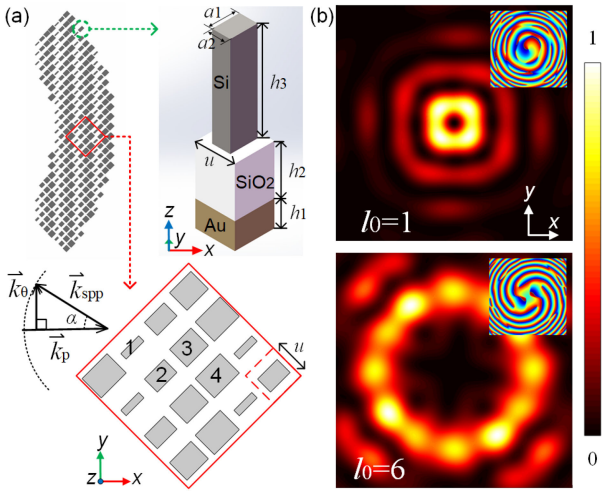

Fig. 3. Construction of OV emitter and patterns of generated OVs. (a) Structure of the QR-PGM. Right and bottom panels show the pixel and unit cell respectively. (b) Cross-sectional intensity distributions of OVs generated by PGM-based emitter. Insets show the phase distributions.

TABLE I
DIMENSIONS OF SILICON NANO-PILLARS

Number	a_1[nm]	a_2[nm]
1	250	75
2	275	182
3	300	245
4	350	270

words, $\boldsymbol{k}_{\mathrm{p}}$ is along the x-direction. As for the value of $\boldsymbol{k}_{\mathrm{p}}$, it can be calculated as $k_{\mathrm{p}} = \pi/(2^{1/2}u)$. When the thicknesses of the gold plate and silica layer are taken as $h_1 = 130$ nm and $h_2 = 500$ nm respectively, the magnitude of SPP wave vector $\boldsymbol{k}_{\mathrm{spp}}$ is equal to that of $\boldsymbol{k}_{\mathrm{p}}$, and an effective SPP emission can be achieved by the PGM. The wave vector used to generate OVs is the sum of $\boldsymbol{k}_{\mathrm{spp}}$ and $\boldsymbol{k}_{\mathrm{p}}$, i.e., $\boldsymbol{k}_{\mathrm{s}} = \boldsymbol{k}_{\mathrm{spp}} + \boldsymbol{k}_{\mathrm{p}}$ (see the wave vector diagram in Fig. 3(a)). There is some discrepancy between $\boldsymbol{k}_{\mathrm{s}}$ and the target vector $\boldsymbol{k}_\theta$ which is equal to $k_{\mathrm{s}}\cos(\alpha/2)\boldsymbol{e}_y$. The symbol $\boldsymbol{e}_y$ denotes the unit vector along the y-axis. However, this discrepancy can be neglected when the incident angle α is small. In our case, the absolute value of angle α is less than 8.3°, and the magnitude ratio of undesired component $k_{\mathrm{s}}\sin(|\alpha|/2)\boldsymbol{e}_x$ to effective one $k_{\mathrm{s}}\cos(|\alpha|/2)\boldsymbol{e}_y$ is less than 8%. The symbol $\boldsymbol{e}_x$ denotes the unit vector along the x-axis.

The ring-shaped emitter was composed by four rotationally equal QR-PGMs, and the inner and outer radius of the emitter were 6.5 μm and 10 μm respectively. Four SPPs with the phase step $\Delta\Phi(l_0)$ and incident angle $\alpha(l_0)$ were fed into QR-PGMs to generate circularly polarized OVs. The phase step and incident angle are calculated as:

$$\Delta\Phi\left(l_0\right) = 2\pi l_0/4 + \Delta\Phi_0, \tag{8}$$

$$\alpha\left(l_0\right) = arcsin\left(\frac{k_\theta}{k_{spp}}\right) = arcsin\left(\frac{\pi l_0}{2\sqrt{2}r_3 k_{spp}}\right). \tag{9}$$

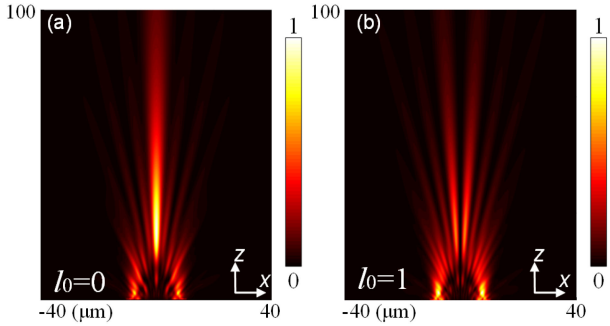

Fig. 4. Comparison between the ordinary light and vortex light emitted by the OV emitter. Side sectional intensity distributions of beams with (a) $l_0 = 0$ and (b) $l_0 = 1$.

where k_{spp} is negative, the positive value of $\Delta\Phi(l_0)$ means the phase increase in anticlockwise direction, $\Delta\Phi_0 = 2\pi/4$, and $r_3 = 8.25$ μm. $\Delta\Phi_0$ is a phase correction factor for the emitted light, and is used to correct the phase that arises from the rotationally symmetry of the four QR-PGMs. The field patterns of generated OVs with $l_0 = 1$ and 6 are shown in Fig. 3(b). Their doughnut-like intensities and vortex-like phases (insets in Fig. 3(b)) clearly indicate the generation of expected OVs.

The free-space OVs generated by the emitter can be regarded as a kind of high-order ring aperture diffraction beams to some extent, which is illustrated by the side sectional intensity distributions (x-z sections) of light in Fig. 4. The area of the x-z section is 80 μm × 100 μm. When the target TC l_0 is taken as zero, the emitted beam has no vortex phase, and its propagation characteristics are similar to that of Gaussian beam. Actually, the emitted light approximates to a ring aperture diffraction beam, as shown in Fig. 4(a). When l_0 is not zero, such as $l_0 = 1$, a dark core is formed in the center of the beam due to the existence of the phase singularity, while the maximum position of the light intensity moves outward, as shown in Fig. 4(b). It can be said that the vortex emitted by the emitter is a kind of high-order ring aperture diffraction beam, i.e., the ring aperture diffraction beam after an azimuthal phase modulation.

Comparing the first panel in Fig. 3(b) with that in Fig. 2(b), it can be found that the circular symmetry of the beam generated by the emitter is low, indicating the low vortex purity. To analyze the vortex purity quantitatively, Eq. (5) is rewritten as:

$$\begin{pmatrix} E_x\left(r,\varphi,z\right) \\ E_y\left(r,\varphi,z\right) \end{pmatrix} = \frac{1}{2\sqrt{\pi}} \sum_{l=-\infty}^{\infty} a_l^{+}(r,z)\exp(il\varphi)\begin{pmatrix} 1 \\ \mathrm{i} \end{pmatrix} + \frac{1}{2\sqrt{\pi}} \sum_{l=-\infty}^{\infty} a_l^{-}(r,z)\exp(il\varphi)\begin{pmatrix} 1 \\ -\mathrm{i} \end{pmatrix}, \tag{10}$$

where

$$\begin{cases} a_l^{+}(r,z) = \frac{1}{2\sqrt{\pi}}\int_0^{2\pi}[E_x(r,\varphi,z) - iE_y(r,\varphi,z)] \\ \qquad \times exp(-il\varphi)d\varphi \\ a_l^{-}(r,z) = \frac{1}{2\sqrt{\pi}}\int_0^{2\pi}[E_x(r,\varphi,z) + iE_y(r,\varphi,z)] \\ \qquad \times exp(-il\varphi)d\varphi \end{cases}, \tag{11}$$

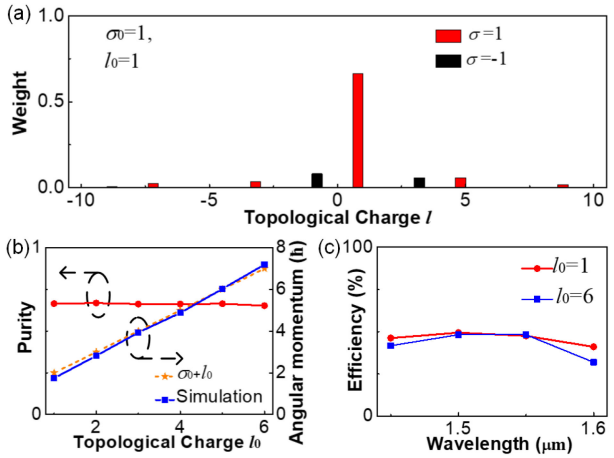

Fig. 5. Vortex spectra, vortex purities, angular momentums and effective efficiency of OVs generated by the OV emitter. (a) Vortex spectrum of the beam corresponding to $\sigma_0 = 1$ and $l_0 = 1$. (b) Purities and angular momentums of emitted OVs. (c) Effective efficiency of emitted OVs within wavelength range of 1.45 μm to 1.6 μm.

The weight of each circularly polarized harmonic is calculated as:

$$\begin{cases} P_l^+ = \dfrac{\int_0^\infty \left|a_l^+(r,z)\right|^2 r\mathrm{d}r}{\int_0^\infty \int_0^{2\pi} \left[|E_x(r,\varphi,z)|^2+|E_y(r,\varphi,z)|^2\right] r\mathrm{d}\varphi\mathrm{d}r} \\ P_l^- = \dfrac{\int_0^\infty \left|a_l^-(r,z)\right|^2 r\mathrm{d}r}{\int_0^\infty \int_0^{2\pi} \left[|E_x(r,\varphi,z)|^2+|E_y(r,\varphi,z)|^2\right] r\mathrm{d}\varphi\mathrm{d}r} \end{cases}. \tag{12}$$

where the superscript "+" and "−" denote left-circular and right-circular polarization respectively. In our case, left-circular polarization is the target polarization, and the vortex purity $P_{l_0}^+$ can be calculated by substituting $l = l_0$ into the first equation in (12). The vortex spectrum of the beam corresponding to $\sigma_0 = 1$ and $l_0 = 1$ is shown in Fig. 5(a), where σ_0 is the spin angular momentum (SAM) order of target OVs and SAM orders $\sigma = 1$ and -1 correspond to left-circular and right-circular polarization respectively. The purity of the emitted OV is 67%, while the theoretical limit can reach 99% (refer to Fig. 2(c)). The low purity is partly due to the incomplete polarization conversion of PGMs, as shown by the undesired polarization harmonics (black) in Fig. 5(a), and a polarization selection procedure can be used to increase vortex purity. After filtering out the right-circular polarized light, the vortex purity of the beam corresponding to $l_0 = 1$ can be increased to 80%. The other factor contributing to low purity is the non-uniform intensity distribution of the SPP, i.e., Gaussian-like intensity distribution (refer to Fig. 1). Non-uniform intensity distributions of incident SPPs ultimately result in the low circular symmetry of the emitted OV, thus the low vortex purity. For the incident wave propagating in finite spatial width, this problem is inevitable.

The angular momentum (AM) of the emitted OV was also investigated. In general, the mean value of the AM per photon can be calculated as [1]:

$$M = k\frac{J}{P}\hbar, \tag{13}$$

where J is the total axial AM flux, P is the total axial linear momentum flux, $\hbar$ is the reduced Planck constant. For beams with rotational symmetry, J/P is expressed as:

$$\frac{J}{P} = \frac{\int_0^\infty \int_0^{2\pi} rS_\varphi(r,\varphi,z)r\mathrm{d}\varphi\mathrm{d}r}{\int_0^\infty \int_0^{2\pi} S_z(r,\varphi,z)r\mathrm{d}\varphi\mathrm{d}r}. \tag{14}$$

where S_φ and S_z are the values of azimuthal and axial time-averaged Poynting vector respectively. The AMs of emitted OVs and their vortex purities are shown in Fig. 5(b). Although the emitted beams possess low OV purities ($\leq$ 67%), their AMs agree well with the simple formula $\sigma_0 + l_0$, where $\sigma_0 = 1$. Further analysis involves the separation of the AM into its spin and orbital parts, but it is beyond the scope of this paper. Readers interested in SAM, OAM and their relationship can refer to references [37]–[39].

Up to this point, only wavelength of 1.55 μm has been involved. To investigate the bandwidth of the OV emitter, the effective efficiency of emitted OVs is calculated within the wavelength range of 1.45 μm to 1.6 μm, and the results are shown in Fig. 5(c). The effective vortex emission efficiency is defined as the product of the radiation efficiency of the emitter and the vortex purity. The simulation shows that the effective vortex emission efficiency of the emitter is around 45% in the TC range of $|l_0| \leq 6$ and wavelength range of 1.45 μm to 1.55 μm (only the effective efficiency of the OVs with $l_0 = 1$ and $l_0 = 6$ is shown in Fig. 5(c)). This wavelength range is enough to cover S and C communication bands. It is not surprising that the PGM-based OV emitter exhibits wide bandwidth given that the optical modulation of silicon nanopillars is non resonant [35].

In a further design, on-chip lenses and cascaded Mach-Zehnder interferometers can be integrated with the OV emitter to achieve high speed OV modulation. The on-chip lenses here are used to transform light waves released from different waveguide ports to parallel waves with different emergent angles [40], and the Mach-Zehnder interferometers are used to switch the optical field among different waveguide channels. The proposed OV emitter is expected to be used in the OV encoding communication [7], [8].

IV. Conclusion

In conclusion, we proposed a compact on-chip OV generator and theoretically demonstrated the effective OV generation. The OV generation of the device is based on the WV-method which was investigated thoroughly. Vortex spectrum analyses showed that WV-method is excellent in generating high-purity vortices even with small number of segments, making it more suitable for chip-scale OV generation. Adjusting silicon pillar dimensions enables an effective wave vector control. Based on this, the QR-PGM was designed. Four QR-PGMs composed the OV emitter which, as a bridge, links different free-space OVs with SPPs incident in different directions. FEM simulations showed that, in the TC range of $|l_0| \leq 6$ and the wavelength range of 1.45 μm to 1.55 μm, the effective vortex emission efficiency of the emitter is around 45%. The proposed device can be used to convert angle coded information into TC coded information. Conversely, this device can be used as a receiver for TC discrimination (see Appendix). Furthermore, the emitter is expected to seed fiber OV modes for long-distance communication [41], [42].

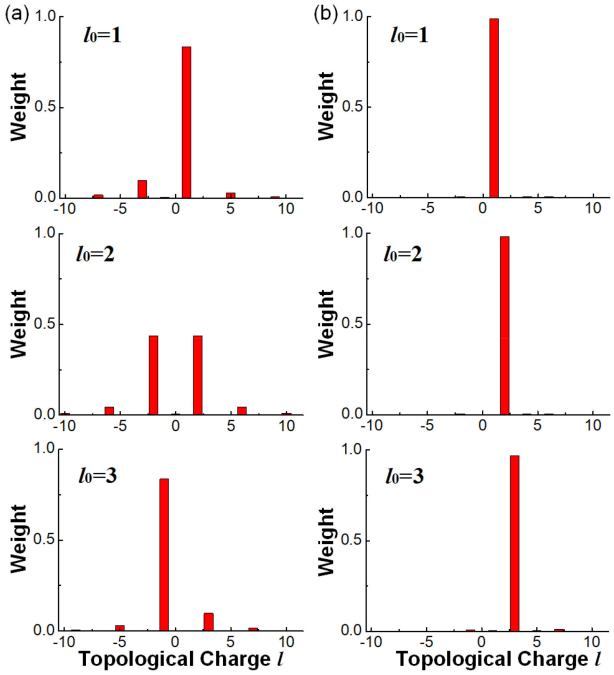

Fig. 6. Vortex spectra. Vortex spectra of the beams generated by (a) P-method and (b) WV-method.

The proposed device, with features of compactness, wide bandwidth, large OV channel capacity and capabilities of fast OV modulation, is very promising for inter-chip WDM-compatible OV communication. This work also shows the great prospect of on-chip application of metasurfaces.

APPENDIX

The topological charge (TC) limit of P-method can be clearly seen by vortex spectra. The vortex spectra of beams generated by P-method are shown in Fig. 6(a). Here, parameters $\{N = 4,\ r_1 = 6.5\ \mu\text{m},\ r_2 = 10\ \mu\text{m}\}$ were adopted. There is just no principal maximum in the vortex spectrum of target TC $l_0 = 2$. This spectrum is symmetry about point of $l = 0$. In the case of $l_0 = 3$, the spectrum shows that the principal maximal harmonic possesses the TC of -1. Actually, the spectrum of $l_0 = 3$ is the same as that of $l_0 = -1$, which is not surprising given that the phase step $\Delta\Phi(l_0 = 3)$ is equal to the step $\Delta\Phi(l_0 = -1)$ under the condition $N = 4$ (refer to the main text for the expression of $\Delta\Phi(l_0)$). For comparison, the vortex spectra of beams generated by WV-method are shown in Fig. 6(b). The same parameters as P-method were used. All spectra show the high vortex purities which are more than 96%. It is clear that WV-method is superior to P-method in optical vortex (OV) generation.

The proposed PGM-based OV emitter can also act as a receiver to decompose OVs into obliquely outgoing SPPs. In this process, the different TCs of OVs correspond to different outgoing angles of SPPs. The OV discrimination capability of the PGM-based device can be explained by the wave vector manipulation as shown in Fig. 7(a). In Fig. 7(a), the black quarter-circle arc denotes the middle of the QR-PGM, the black lines with arrows denote the structural wave vector $\boldsymbol{k}_{\mathrm{p}}$ of the

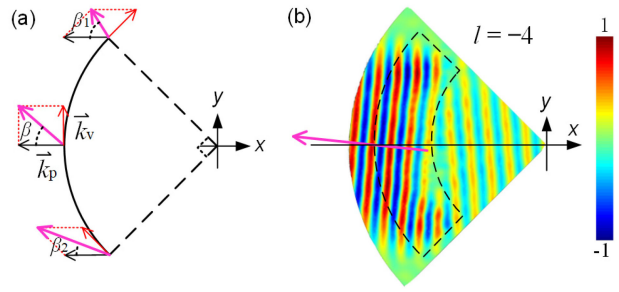

Fig. 7. Topological charge discrimination. (a) Schematic diagram of the vortex discrimination. (b) Normalized electric field of SPPs excited by optical vortex with $l = -4$.

QR-PGM, and the red lines with arrows denote the wave vector $\boldsymbol{k}_{\mathrm{v}}$ which is induced by the incident vortex beams. $\boldsymbol{k}_{\mathrm{p}}$ is along the negative x-direction in this case, and its magnitude equals to that of $\boldsymbol{k}_{\mathrm{spp}}$ (wave vector of SPP) of $\lambda = 1.55\ \mu$m. $\boldsymbol{k}_{\mathrm{v}}$ is along the arc, and its positive direction is determined as the anticlockwise direction. The value of $\boldsymbol{k}_{\mathrm{v}}$ is calculated as $k_{\mathrm{v}} = l/r_{\mathrm{mid}}$, where l is the TC of the incident vortex beams, and r_{mid} is the radius of the black arc. It is clear that the sum of $\boldsymbol{k}_{\mathrm{p}}$ and $\boldsymbol{k}_{\mathrm{v}}$ (magenta lines with arrows in Fig. 7(a)) is ultimately responsible for the excitation of SPPs. The oblique angle of the excited SPPs can be calculated as:

$$\beta = \arctan\left(\frac{l}{r_{\mathrm{mid}} k_{\mathrm{p}}}\right). \tag{15}$$

where k_{p} is the value of vector $\boldsymbol{k}_{\mathrm{p}}$, and it is positive. It should be noted that (15) is actually the oblique angle of the SPP emerged from the central of the QR-PGM, and the SPPs as a whole are not perfect parallel light beams (as shown by magenta lines with arrows in Fig. 7(a)). However, in our case, i.e., $|l_0| \leq 6$, the divergence of the SPP beams is small, and the SPPs can be regarded as parallel waves approximately. Specifically, the divergence angle of SPP beams is proportional to $|l_0|$, and the divergence angle at $|l_0| = 6$ is around 2.6°C. For a demonstration, the simulation with a QR-PGM and a normal incident vortex beam is carried out. The electric field of excited SPPs is shown in Fig. 7(b), and the black dashed box in Fig. 7(b) denotes the position of QR-PGM. Here, the Bessel beam with $\sigma = -1$ and $l = -4$ is used as the incident vortex beam, and the position of the maximum intensity of Bessel beam is alignment with the middle of the QR-PGM. The simulation shows that the oblique angle of the SPP beam is around -5.2°C. This value agrees well with -5.0°C which is calculated by (15).

REFERENCES

[1] L. Allen, M. W. Beijersbergen, R. J. C. Spreeuw, and J. P. Woerdman, "Orbital angular momentum of light and the transformation of Laguerre–Gaussian laser modes," *Phys. Rev.* vol. 45, no. 11, pp. 8185–8189, 1992.
[2] Y. J. Shen *et al.*, "Optical vortices 30 years on: OAM manipulation from topological charge to multiple singularities," *Light-Sci. Appl.*, vol. 8, no. 1, 2019, Art. no. 90.
[3] N. B. Simpson, K. Dholakia, L. Allen, and M. J. Padgett, "Mechanical equivalence of spin and orbital angular momentum of light: An optical spanner," *Opt. Lett.*, vol. 22, no. 1, pp. 52–54, 1997.
[4] D. G. Grier, "A revolution in optical manipulation," *Nature*, vol. 424, no. 6950, pp. 810–816, 2003.

[5] J. Hamazaki, R. Morita, K. Chujo, Y. Kobayashi, S. Tanda, and T. Omatsu, "Optical-vortex laser ablation," *Opt. Exp.*, vol. 18, no. 3, pp. 2144–2151, 2010.

[6] M. Duocastella and C. B. Arnold, "Bessel and annular beams for materials processing," *Laser Photon. Rev.*, vol. 6, no. 5, pp. 607–621, 2012.

[7] G. Gibson *et al.*, "Free-space information transfer using light beams carrying orbital angular momentum," *Opt. Exp.*, vol. 12, no. 22, pp. 5448–5456, 2004.

[8] A. J. Willner *et al.*, "Experimental demonstration of 20 Gbit/S data encoding and 2 ns channel hopping using orbital angular momentum modes," *Opt. Lett.*, vol. 40, no. 24, pp. 5810–5813, 2015.

[9] J. Wang *et al.*, "Terabit free-space data transmission employing orbital angular momentum multiplexing," *Nat. Photon.*, vol. 6, no. 7, pp. 488–496, 2012.

[10] N. Bozinovic *et al.*, "Terabit-Scale orbital angular momentum mode division multiplexing in fibers," *Science*, vol. 340, no. 6140, pp. 1545–1548, 2013.

[11] A. Mair, A. Vaziri, G. Weihs, and A. Zeilinger, "Entanglement of the orbital angular momentum states of photons," *Nature*, vol. 412, no. 6844, pp. 313–316, 2001.

[12] R. Fickler, R. Lapkiewicz, M. Huber, M. P. J. Lavery, M. J. Padgett, and A. Zeilinger, "Interface between path and orbital angular momentum entanglement for high-dimensional photonic quantum information," *Nat. Commun.*, vol. 5, 2014, Art. no. 4502.

[13] M. Mirhosseini *et al.*, "High-dimensional quantum cryptography with twisted light," *New J. Phys.*, vol. 17, 2015, Art. no. 033033.

[14] M. W. Beijersbergen, R. P. C. Coerwinkel, M. Kristensen, and J. P. Woerdman, "Helical-wavefront laser beams produced with a spiral phaseplate," *Opt. Commun.*, vol. 112, no. 5-6, pp. 321–327, 1994.

[15] M. I. Shalaev, J. B. Sun, A. Tsukernik, A. Pandey, K. Nikolskiy, and N. M. Litchinitser, "High-efficiency all-dielectric metasurfaces for ultracompact beam manipulation in transmission mode," *Nano Lett.*, vol. 15, no. 9, pp. 6261–6266, 2015.

[16] M. B. Pu *et al.*, "Catenary optics for achromatic generation of perfect optical angular momentum," *Sci. Adv.*, vol. 1, no. 9, 2015, Art. no. 1500396.

[17] S. Q. Chen, W. W. Liu, Z. C. Li, H. Cheng, and J. G. Tian, "Metasurface-Empowered optical multiplexing and multifunction," *Adv. Mater.*, vol. 32, no. 3, 2020, Art. no. 1805912.

[18] T. H. Su *et al.*, "Demonstration of free space coherent optical communication using integrated silicon photonic orbital angular momentum devices," *Opt. Exp.*, vol. 20, no. 9, pp. 9396–9402, 2012.

[19] B. B. Guan *et al.*, "Free-space coherent optical communication with orbital angular, momentum multiplexing/demultiplexing using a hybrid 3D photonic integrated circuit," *Opt. Exp.*, vol. 22, no. 1, pp. 145–156, 2014.

[20] X. L. Cai *et al.*, "Integrated compact optical vortex beam emitters," *Science*, vol. 338, no. 6105, pp. 363–366, 2012.

[21] S. M. Li *et al.*, "Orbital angular momentum vector modes (de)multiplexer based on multimode micro-ring," *Opt. Exp.*, vol. 26, no. 23, pp. 29895–29905, 2018.

[22] Z. W. Xie *et al.*, "Ultra-broadband on-chip twisted light emitter for optical communications," *Light-Sci. Appl.*, vol. 7, 2018, Art. no. 18001.

[23] S. L. Sun, Q. He, S. Y. Xiao, Q. Xu, X. Li, and L. Zhou, "Gradient-index meta-surfaces as a bridge linking propagating waves and surface waves," *Nat. Mater.*, vol. 11, no. 5, pp. 426–431, 2012.

[24] S. L. Sun *et al.*, "High-efficiency broadband anomalous reflection by gradient meta-surfaces," *Nano Lett.*, vol. 12, no. 12, pp. 6223–6229, 2012.

[25] W. J. Sun, Q. He, S. L. Sun, and L. Zhou, "High-efficiency surface plasmon meta-couplers: Concept and microwave-regime realizations," *Light-Sci. Appl.*, vol. 5, no. 1, 2016, Art. no. 16003.

[26] Z. Y. Li *et al.*, "Controlling propagation and coupling of waveguide modes using phase-gradient metasurfaces," *Nat. Nanotechnol.*, vol. 12, no. 7, pp. 675–683, 2017.

[27] N. F. Yu *et al.*, "Light propagation with phase discontinuities: Generalized laws of reflection and refraction," *Science*, vol. 334, no. 6054, pp. 333–337, 2011.

[28] R. K. Luneburg, *Mathematical Theory of Optics*. Los Angeles, CA, USA: Univ. California Press, 1964, pp. 313–316.

[29] S. Guha and G. D. Gillen, "Description of light propagation through a circular aperture using nonparaxial vector diffraction theory," *Opt. Exp.*, vol. 13, no. 5, pp. 1424–1447, 2005.

[30] G. Molina-Terriza, J. P. Torres, and L. Torner, "Management of the angular momentum of light: Preparation of photons in multidimensional vector states of angular momentum," *Phys. Rev. Lett.*, vol. 88, no. 1, 2002, Art. no. 013601.

[31] C.-S. Guo, D.-M. Xue, Y.-J. Han, and H. Ding, "Optimal phase steps of multi-level spiral phase plates," *Opt. Commun.*, vol. 268, no. 2, pp. 235–239, 2006.

[32] J. Du and J. Wang, "High-dimensional structured light coding/decoding for free-space optical communications free of obstructions," *Opt. Lett.*, vol. 40, no. 21, pp. 4827–4830, 2015.

[33] Y. Hu, S. Fu, H. Yin, Z. Li, Z. Li, and Z. Chen, "Subwavelength generation of nondiffracting structured light beams," *Optica*, vol. 7, no. 10, pp. 1261–1266, 2020.

[34] COMSOL Multiphysics, V 5.4, [Online]. Available: https://cn.comsol.com/productdownload/5.4/windows

[35] M. Khorasaninejad and K. B. Crozier, "Silicon nanofin grating as a miniature chirality-distinguishing beam-splitter," *Nat. Commun.*, vol. 5, 2014, Art. no. 5386.

[36] A. Arbabi, Y. Horie, M. Bagheri, and A. Faraon, "Dielectric metasurfaces for complete control of phase and polarization with subwavelength spatial resolution and high transmission," *Nat. Nanotechnol.*, vol. 10, no. 11, pp. 937–944, 2015.

[37] S. M. Barnett *et al.*, "On the natures of the spin and orbital parts of optical angular momentum," *J. Opt.*, vol. 18, no. 6, 2016, Art. no. 064004.

[38] K. Y. Bliokh, J. Dressel, and F. Nori, "Conservation of the spin and orbital angular momenta in electromagnetism," *New J. Phys.*, vol. 16, 2014, Art. no. 093037.

[39] M. F. Picardi, K. Y. Bliokh, F. J. Rodriguez-Fortuno, F. Alpeggiani, and F. Nori, "Angular momenta, helicity, and other properties of dielectric-fiber and metallic-wire modes," *Optica*, vol. 5, no. 8, pp. 1016–1026, 2018.

[40] Z. Wang, T. T. Li, A. Soman, D. Mao, T. Kananen, and T. Y. Gu, "On-chip wavefront shaping with dielectric metasurface," *Nat. Commun.*, vol. 10, 2019, Art. no. 3547.

[41] J. F. Ye *et al.*, "Generating broadband vortex modes in ring-core fiber by using a plasmonic q-plate," *Opt. Lett.*, vol. 42, no. 16, pp. 3064–3067, 2017.

[42] J. Liu *et al.*, "Direct fiber vector eigenmode multiplexing transmission seeded by integrated optical vortex emitters," *Light-Sci. Appl.*, vol. 7, 2018, Art. no. 17148.